PAPER

Check for updates

Utilizing 2D metal halide perovskite thin films as highly tuneable surfaces for orientation control of energetic materials†

Natalie Smith-Papin,[a] Meagan Phister,[a] Ashley Conley, [iD][a] Nathan Swami, [iD][b] Zbigniew Dreger[c] and Gaurav Giri [iD]*[a]

The development of high performing and stable energetic materials (EMs) is a focus for a variety of applications including explosives, propellants, and pyrotechnics. To enhance stability, energetic crystals are often interfaced with materials such as chemical binders, which can introduce a variety of physiochemical phenomena ultimately leading to unpredictable stability and performance within the composite. Therefore, a thorough understanding of how energetic crystals behave when interfaced with various chemical functionalities is crucial for designing safer, high performing energetic formulations. This work provides a fundamental insight into interactions between a high performing energetic material, CL-20 (hexanitrohexaazaisowurtzitane), and other materials' surfaces. Highly controlled, tunable 2D metal-halide perovskite (2D MHP) templates with tunable periodicity and chemistry were created and used as a template layer to influence nucleation and growth of CL-20 crystals. All MHP/CL-20 bilayer films exhibit small, nonuniform crystalline deposit morphology for the CL-20 crystals with β-CL-20 polymorphic structure. While most MHP films template the formation of β-CL-20 crystals with a (111) preferential orientation, $PbPMA_2Cl_4$/β-CL-20 films crystallize with a (020) preferential orientation. The results presented herein suggest interfacial energy minimization between the two bilayer components is the dominant driving force behind the CL-20 preferential orientations. This methodology can potentially be used for developing techniques for growing energetic crystals with desired morphology, packing density and crystallographic orientation.

Introduction

The development of energetic materials (EMs) with a balance between high performance and stability is challenging, but critically important for advancing military and space applications. CL-20, named after its place of discovery in China Lake,[1] has the highest known energy density, detonation velocity, and detonation pressure,[2] making CL-20 a benchmark state-of-the-art material in the field of energetic materials.[3] However, limitations relating to its high impact sensitivity and facile phase transformation between its ambient-stable polymorphic phases (β, ε, and γ) have hindered commercialization of CL-20.[4,5] For other EMs, such as HMX, polymers have been employed to modulate and template EM nucleation and growth to enhance material properties including stability and performance.[6,7]

To improve upon the understanding of CL-20 crystallization and phase formation, previous work from our group has employed a meniscus-guided coating (MGC) technique that provides a high degree of control over the crystallization pathway of CL-20 thin films,[8] similar to other organic small molecules.[9–13] In addition to controlling the crystallization pathway through evaporative coating, self-assembled monolayers (SAMs) are a common approach used in a variety of fields, including organic optoelectronics and catalysis, to template nucleation and growth of crystalline materials. SAMs have been shown to influence thin film morphology, polymorphism, phase purity, and crystallographic orientation in thin film geometry by providing variable surface energy and topography for heterogeneous nucleation to occur.[14–19] Specific to CL-20, Urbelis et al. studied the influence of homogeneous nucleation of CL-20 in various solvent systems,[20] as well as the effect of heterogeneous nucleation of CL-20 on SAMs with various chemical moieties.[21] This work demonstrated that different surface moieties stabilize different polymorphic structures and preferred growth habits/orientations.

[a] Department of Chemical Engineering, University of Virginia, Charlottesville, Virginia, 22904, USA. E-mail: gg3qd@virginia.edu

[b] Department of Electrical and Computer Engineering, University of Virginia, Charlottesville, Virginia, 22904, USA

[c] RDT&E Department, Naval Surface Warfare Center Indian Head Division, Indian Head, Maryland, 20640, USA

3248 | React. Chem. Eng., 2024, **9**, 3248–3256

This journal is © The Royal Society of Chemistry 2024

While SAMs have proven useful in influencing nucleation and growth of organic crystals, SAMs are limited because the ligand density is not easily controlled, and SAMs generally form an amorphous layer on the substrate.[19] Density and order of these terminating functional groups play a major role in influencing the surface energy and interfacial interactions present in bilayer materials.[20] Recently, one layer ($n = 1$) hybrid two-dimensional (2D) metal halide perovskites (2D MHPs), have been utilized as a novel approach to create a periodic and chemically tuneable SAM surface for organic molecule crystallization.[22,23] Xiao *et al.* used chemical vapor deposition of an organic semiconducting molecule on top of a 2D MHP surface and observed a high degree of preferential orientation of the organic layer, attributed to the highly controlled perovskite template layer.[24] Conley *et al.* employed MGC to coat a semiconducting organic molecule atop several one layer ($n = 1$) 2D MHPs with unique surface compositions and observed polymorphism and increased order in the organic crystals, which were attributed to the interfacial interactions between the organic molecule and MHP.[25]

Further, recent work has focused on elucidating principles governing organic heteroepitaxial interfaces. Epitaxial growth in inorganic materials is governed by strong covalent or ionic interactions, which only allow for a small degree of lattice mismatch before dislocations arise to relieve strain at the bilayer interface. However, for organic crystalline interfaces, weaker, noncovalent interactions allow for larger degrees of lattice mismatch for heteroepitaxial growth.[26] As the 2D MHPs preferentially orient with the organic ligand at the terminating surface, we consider this surface as a pseudo-organic crystalline substrate. Additionally, 2D MHPs are highly tuneable in the sense that varying the components (*e.g.* ligand, halide) results in a variation of the crystal lattice parameters. By utilizing 2D MHP surfaces with varying lattice parameters,[25] bilayer crystallization of organic molecules on perovskite surfaces provides a promising platform to probe the governing mechanisms of organic molecule heteroepitaxial nucleation and growth.

Dull *et al.* recently found that organic crystalline heteroepitaxial growth in a variety of lattice matched template/overlayer pairs occurs only if the overlayer crystallographic plane that is lattice matched is the lowest surface energy bulk crystal face.[27] Others have studied the organic/organic epitaxial growth through vapor deposition of multiple crystalline pairs,[28,29] but most work studies molecular crystal overlayers relevant for semiconductor applications that exhibit π–π stacking (rubrene, pentacene, tetracene) atop a crystalline template that also shows π–π stacking behaviour.[26,27,29] To the best knowledge of the authors, no previous work has probed interfacial interactions between the underlayer and the molecular crystals where neither layer shows π-stacking characteristics, underlying the novelty of the presented work.

In this work, MGC of CL-20 on top of a slate of highly controlled, tuneable 2D MHP templates was explored to influence nucleation and growth of CL-20 crystals, ultimately impacting morphology, crystal packing density, and preferential orientation. While the morphology of CL-20 remained consistent across all bilayer films, changes in the MHP template led to the observation of two distinct preferential orientations of CL-20.

Crystal properties, such as morphology and preferential orientation, play a pivotal role in influencing the sensitivity and stability of energetic materials. The ability to exercise precise control over these properties allows us to engineer materials with specific initiation and decomposition characteristics. By tailoring the behaviour of energetic crystals, we open avenues for substantial improvements in device performance and safety.

Materials & methods

Materials

Silicon wafers with native oxide surface and crystallographic orientation $\langle 1\ 0\ 0 \rangle$ were sourced from University Wafer. Trichloro(octadecyl)silane (OTS, >90%) used for coating blade functionalization was sourced from Sigma Aldrich. Perovskite materials, including lead chloride (PbCl$_2$, Sigma Aldrich, 99.999%), lead bromide (PbBr$_2$, Sigma Aldrich, 99.99%), phenylethyl ammonium chloride (PEACl, Sigma Aldrich, ≥98%), phenylethyl ammonium bromide (PEABr, Sigma Aldrich, ≥98%), phenylmethyl ammonium chloride (PMACl, Sigma Aldrich, ≥98%), and phenylmethyl ammonium bromide (PMABr, Sigma Aldrich, ≥98%) were used as received. Dimethyl sulfoxide (DMSO, anhydrous, Sigma Aldrich, ≥99.9%), *N-N*-dimethylacetamide (DMAc, anhydrous, Sigma Aldrich, ≥99.8%), ethyl acetate (Fisher Scientific, 99.9%), toluene (Sigma Aldrich, 99.5%), isopropanol (Fisher Chemical, 99.5%), and acetone (Fisher Chemical, 99.7%) were used as received. 2,4,6,8,10,12-hexanitrohexaazaisowurtzitane (ε-CL-20) was sourced from the Naval Surface Warfare Center Indian Head Division and used as received.

Substrate preparation

Substrates were cut to 1 in. × 1 in. squares and sonicated for 10 minutes sequentially in an aqueous detergent solution, deionized water, isopropanol, and acetone. Substrates were then dried under a compressed air stream and placed in a BioForce Nanosciences UV Ozone cleaner for 10 minutes. After removing from the UV Ozone cleaner, substrates were immediately put into a glovebox before spincoating perovskite precursor solution.

Perovskite precursor solution making

All lead halide perovskite precursor solutions were prepared using the formula A$_2'$PbX$_4$ where A$'$ = organic ligand (phenylethyl ammonium, phenylmethyl ammonium) and X = halide ion (chloride, bromide) in an LC Technology Solutions Inc. nitrogen glovebox environment. All solutions were made with a 0.375 M concentration with respect to the lead

component. For instance, the $Pb(PMA)_2Cl_4$ solution was prepared with 0.375 M $PbCl_2$ and 0.75 M PMACl. The chloride-based perovskite precursor solutions were prepared with DMSO as the solvent, and the bromide solutions with DMAc. Solutions stirred overnight in the glovebox prior to spincoating.

Perovskite spincoating

Cleaned silicon substrates were placed onto a Specialty Coatings Systems Inc. spincoater in the glovebox. 45 µL of the perovskite precursor solution was pipetted onto the substrate after 4500 RPM was reached. The film maintained 4500 RPM for 60 seconds after solution deposition. After dynamically spincoating, thin films were immediately moved to a hot plate for thermal annealing at 100 °C for five minutes.

Meniscus-guided coating blade preparation

A silicon wafer was cut into a 4 cm × 3 cm rectangle with the flat side intended as a contact edge for coating. The blade was sonicated sequentially in water, toluene, isopropanol, and acetone for 10 minutes each. After drying under an air stream and placing in a BioForce Nanosciences UV Ozone cleaner for 20 minutes, the blade was submerged in a large crystallization dish containing an OTS/toluene solution of 200 µL per 50 mL. The dish was heated at 50 °C and stirred for 20 hours to allow the OTS to chemisorb onto the silicon surface. The blade was removed from the dish, dried, and sonicated in acetone for 10 minutes to remove any physisorbed material.

Meniscus-guided coating technique

Thin films of CL-20 were crystallized using an in-house meniscus-guided coating technique. An aluminium block (designed in-house, machined by Protolabs), was interfaced with high temperature heating cartridges (McMaster-Carr), and J-type thermocouples (McMaster-Carr) were utilized to maintain a constant, setpoint temperature of the aluminium block. A blade holder with angle/yaw (OptoSigma) and height (Edmunds Optics) micromanipulators to adjust the blade position relative to the aluminium block. The blade holder was attached to a linear driver (Zaber Technology) to translate the coating blade at a fixed speed relative to the substrate. A vacuum connection was machined into the aluminium block to hold the sample in place during coating.

The MGC technique was utilized to crystallize CL-20 on top of the perovskite surfaces. A solution containing 30 mg mL^{-1} of CL-20 in ethyl acetate was prepared. 50 µL of this solution was pipetted between the coating blade and the silicon/perovskite film, before the blade began translating at 0.05 mm s^{-1} across the film. All films were crystallized at room temperature (20 °C). MGC conditions were held constant during this study, only the perovskite underlayer was changed.

Solvent vapor annealing

The solvent vapor annealing chamber consists of a large crystallization dish containing a platform. 50 mL of ethyl acetate was added to the bottom of the chamber such that it did not contact the top of the platform. The CL-20 films were placed on top of the platform and the chamber was covered to create an environment saturated with ethyl acetate vapor. Films were annealed for 8 minutes before removing for further characterization.

Optical imaging

A Zeiss Axio Imager A.1 optical microscope (Carl Zeiss AG) with a Zeiss Axiocam 503 Color camera (Carl Zeiss AG) was utilized to image the 2D MHP and 2D MHP/CL-20 films. Images were collected at 5×, 10×, 20×, and 50× magnification and under both optical and cross polarized light.

Profilometry

A Bruker DektakXT stylus profilometer was utilized to measure film thickness with a scan speed of 10 µm s^{-1} and a stylus force of 3 mg. A razor blade was used to remove a slice of the film, exposing the silicon underlayer. The stylus measured several hundred microns of the film before falling off the ledge and onto the substrate. The average height difference was measured between the films and the substrate to determine the film thickness.

Raman spectroscopy

A Renshaw inVia confocal Raman microscope (spatial resolution <2 µm and spectral resolution 0.3 cm^{-1}) with a 514 nm laser and 1800 l mm^{-1} grating was utilized to measure the Raman shift (100–3500 cm^{-1}) for each film at three locations. Data were collected with 8 second exposure and 8 accumulations.

Atomic force microscopy

A Bruker Innova atomic force microscope was used to collect data on the surface topology of the bilayer films. Tapping mode was used to measure 2 µm × 2 µm regions with 512 × 512 lines and a scan speed of 0.5 µm s^{-1}.

X-ray diffraction

A Rigaku SmartLab diffractometer in Bragg–Bretano scanning geometry was also used to obtain diffraction patterns. X-rays were generated using Cu Kα radiation and accelerated at 45 kV voltage. A beam current of 40 mA was used, and films were measured from 5–20 (° 2θ).

Results and discussion

2D metal halide perovskite (2D MHP) structures with one-layer dimensionality (n = 1) were chosen, and due to the packing geometry, the films crystallize with surface termination of the organic ligand at the interface (Fig. 1a).[22]
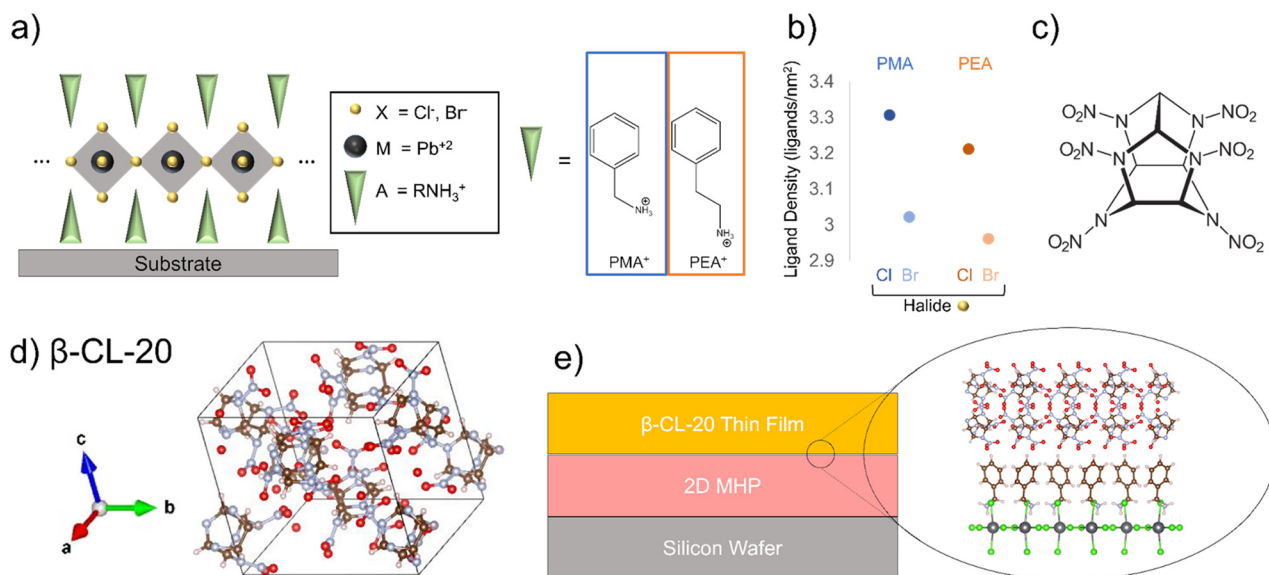
3250 | React. Chem. Eng., 2024, 9, 3248–3256

This journal is © The Royal Society of Chemistry 2024

Fig. 1 (a) Schematic of the structure of (n = 1) 2D metal halide perovskites, (b) ligands of interest in this study, including PMA$^+$ and PEA$^+$ and their respective density on the 2D MHP surface as a function of changing perovskite halide, (c) molecular structure of CL-20, (d) crystal structure of β-CL-20,[1] e) schematic depicting EM-2D MHP interface. VESTA software[30] was used for crystal structure graphics.

We chose to create four 2D MHP films, containing Pb^{2+} as the divalent metal atom (M), Cl$^-$ and Br$^-$ as the halide (X), and phenylmethyl amine (PMA) and phenylethyl amine (PEA) as the organic cation (A′) components. Optical images of the 2D MHP after spincoating and thermal annealing show the expected 2D MHP film morphology prior to bilayer deposition (ESI† Fig. S1).[25]

Comparing the fabricated 2D MHP films to their respective simulated diffraction patterns for each 2D MHP chosen[31–34] we find that the spincoated 2D MHP films preferentially crystallize with the octahedra parallel to the silicon surface, exhibiting (200) orientation for PMA-ligand structures and (001) orientation for PEA-ligand structures (Fig. 1a and ESI† Fig. S2). The preferential orientation observed through diffraction confirms the ligand termination at the film surface for all 2D MHPs. Altering the ligand (PMA *vs.* PEA) in the perovskite structure provides control over the orientation of the benzene ring. For PMA-based perovskites, the benzene ring orients perpendicular to the octahedra layer and substrate, while for PEA-based perovskites, the benzene ring orients diagonally with respect to the octahedra layer and substrate (ESI† Fig. S3). Further, altering the halide within the perovskite structure modifies the ligand density on the surface. Chlorine-based perovskites have higher ligand density, due to the smaller size of the chlorine ion, relative to bromine-based perovskites (Fig. 1b, ESI† Table S1).

To effectively employ MGC on top of a 2D MHP film and probe the effects of different interfacial interactions, it is crucial that the solvent chosen for MGC does not alter the 2D MHP crystallinity. Several solvents with sufficient CL-20 (Fig. 1c) solubility were tested to determine compatibility with the 2D MHP films. Through optical microscopy and x-ray diffraction, the morphology of the 2D MHP thin films

and the diffraction peak location due to X-ray scattering from the 2D MHPs are unchanged (ESI† Fig. S4) when contacted with ethyl acetate (EtOAc); therefore, the 2D MHP surfaces are resistant to degradation or changes in crystalline structure when exposed to EtOAc.

For MGC of CL-20 on 2D MHP films, a 30 mg mL^{-1} solution of CL-20 in EtOAc (solubility = 384.2 mg mL^{-1} at 25 °C)[35] was used to achieve a fully covered CL-20 film (Fig. 1e). Polarized optical microscopy shows film morphology of 2D MHP/CL-20 bilayer films (Fig. 2). Optical (left column) and cross-polarized (middle column) images for each bilayer exhibit the formation of nonuniform crystalline deposits of CL-20, a morphology observed in previous MGC studies with glycine,[36] as well as previous studies with CL-20 crystallized from a DMSO-based solution.[8] This behaviour can be explained by stick–slip motion of the meniscus during the coating process, resulting in bands of thick and thin crystalline regions.[37–39] Further, very small and discrete particles of CL-20 are observed for all conditions (Fig. 2).

Film topography and thickness were measured for both 2D MHP and 2D MHP/CL-20 bilayer films using atomic force microscopy (AFM) and profilometry, respectively. AFM images were collected for 2D MHP films (ESI† Fig. S5) and 2D MHP/CL-20 bilayer films (Fig. 2, right column). Film topography at the nanoscale confirms nanocrystallite CL-20 morphology, and similar morphology were seen for all EM grown on the 2D MHP template layers. After crystallization of CL-20 on the 2D MHP surface, thicknesses of bilayer films were 1.4–1.8 μm, compared to the bare 2D MHP film thickness of 150–180 nm (ESI† Fig. S6). Due to stick–slip motion, heterogeneity in the thickness of the CL-20 layer resulted in relatively large standard deviations. Despite this, the average value for thin film thickness is similar between all 2D MHP/CL-20 bilayer films.
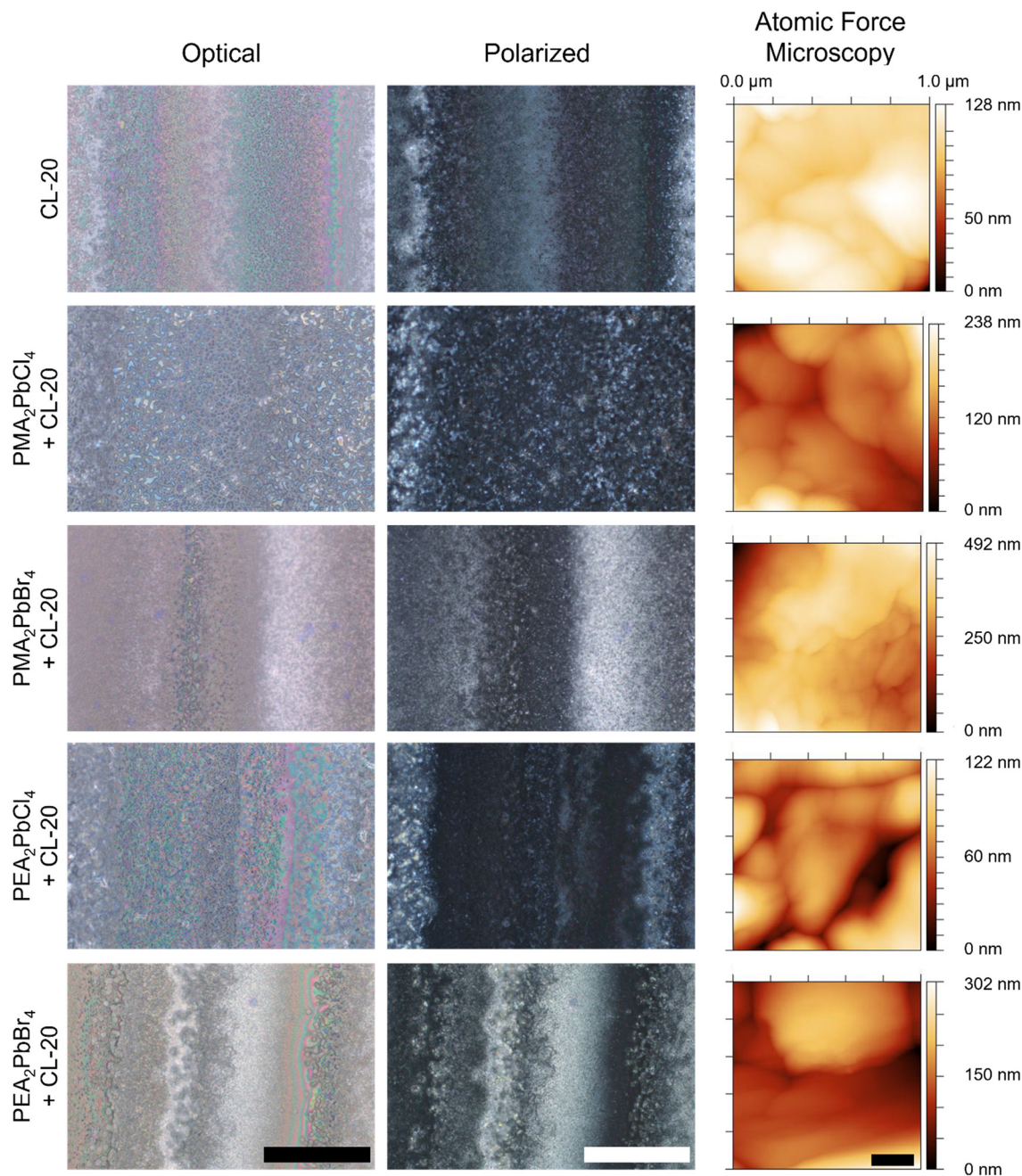
This journal is © The Royal Society of Chemistry 2024

React. Chem. Eng., 2024, **9**, 3248–3256 | **3251**

Fig. 2 Optical (left), cross-polarized optical (middle), and AFM (right) images for bilayer MHP/CL-20 films. Scale bar = 100 μm for all optical images (left, middle). Scale bar = 200 nm for all AFM images (right).

Films were characterized by Raman spectroscopy to analyse differences in vibrational stretching within the crystal structure because of interfacial interactions. These data inform which polymorphic structure of CL-20 has been crystallized. Several peaks (285 cm^{-1} – "cage" stretch, 833 cm^{-1} – ring stretch, 1327 cm^{-1} – symmetric NO_2 stretch, and 3043 cm^{-1} – C–H stretch)[40] were analysed and confirm the preferential crystallization of β-CL-20. Peak location for the bilayer samples was analysed, and no significant peak shifts, indicative of strain in the crystal structure, were observed because of the different underlying 2D MHP templates (ESI† Fig. S7).

Analysis of the XRD data for the 2D MHP/CL-20 films further confirm the polymorphic identity (β-CL-20) of the organic layer of the films (ESI† Fig. S8) and demonstrates the interfacial effects on the resultant CL-20 crystallization. The simulated β-CL-20 pattern (Fig. 3, green)[1] is compared to the CL-20 films coated on the silicon and the MHP templates. The β-CL-20 films coated on silicon exhibit a strong (111) preferential orientation relative to the substrate, indicated by the peak observed at 0.972 Å^{-1} (Fig. 3, black). Based on the relative surface energy of the β-CL-20 crystallographic planes, (020) and (002) planes have the lowest surface energy, while
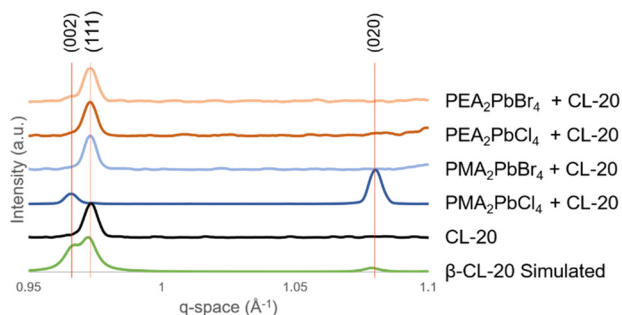
Fig. 3 a) Representative diffraction patterns for various bilayer films relative to the simulated β-CL-20 (green) pattern. (020), (111), and (002) planes are highlighted to denote observed preferential orientation.

the (111) plane exhibits higher surface energy.[21] Typically, the lowest surface energy plane is expected to crystallize oriented with the template surface;[27] therefore, this observation requires further exploration. We propose that the MGC technique may be causing non-equilibrium orientation formation of the crystal, much like how in other organic materials, the MGC technique has shown the stabilization of non-equilibrium polymorphs.[36,41]

For PEA_2PbCl_4, PEA_2PbBr_4, and PMA_2PbBr_4 2D MHP templates, β-CL-20 films also exhibit the (111) preferential orientation (Fig. 3). However, for the PMA_2PbCl_4 2D MHP template, β-CL-20 preferentially orients with the (002) and (020) planes (located at 0.967 $Å^{-1}$ and 1.078 $Å^{-1}$, respectively) parallel to the 2D MHP layer (Fig. 3, dark blue). The average and standard deviations for each diffraction peak location are plotted in ESI† Fig. S9. This behaviour cannot be exclusively attributed to the chemical functionality (orientation of the benzene ring on the surface) or the density of the ligands on the surface, indicating that the unique surface energy/topography of the PMA ligand combined with the chlorine halide (density) is responsible for the distinctive preferential orientation.

We take a closer look at the unit cells of the 2D MHPs and β-CL-20 to explain the orientation changes. The PMA-based 2D MHP films exhibit a (200) preferential orientation relative to the substrate; therefore, the b and c dimensions were considered as they represent the interfacial plane in contact with the β-CL-20 surface. Similarly, for the PEA-based 2D MHP films, with preferential orientation of (001) relative to the substrate, the a and b dimensions were considered. Referencing the lattice matching analysis from Dull *et al.*, for each crystallographic plane of interest in all materials, a rectangle or parallelogram was constructed using two side lengths and one angle from the unit cell (ESI† Fig. S10).[27] Comparing the dimensions of the 2D MHP rectangles to the rectangles/parallelograms associated with the three β-CL-20 planes of interest ((020), (002), (111)), a fit parameter, m, was calculated, where m is defined as: $m = (A_t + A_{O(hkl)} - 2A_i)/A_t$, where A_t is the area of the 2D MHP template rectangle, $A_{O(hkl)}$ is the area of the (hkl) β-CL-20 plane rectangle/parallelogram, and A_i is the area of intersection of the two components

(ESI† Fig. S10). When a perfect lattice match is achieved, $m = 0$.[27] For these 2D MHP/CL-20 crystallographic plane pairs, the calculated m values are listed in Table 1.

With this analysis, all 2D MHP structures have the closest match with the (020) plane of β-CL-20 (lowest m values, highlighted in green). However, experimentally we only observe the PMA_2PbCl_4 template preferentially orient the (020) plane of β-CL-20, while the PMA_2PbBr_4, PEA_2PbCl_4, and PEA_2PbBr_4 templates preferentially orient the (111) plane of β-CL-20 (bolded values). From this analysis, only the PMA_2PbCl_4 films experimentally exhibit the optimized (lowest m value) lattice matching configuration, while all other surfaces preferentially orient the least optimized (highest m value) lattice configuration of the three considered. Interestingly, the PEA-based films have a close lattice match to the lower surface energy β-CL-20 crystallographic plane ((020), $m < 0.18$), but this template preferentially crystallizes the (111) orientation. Ultimately, we do not see an optimized lattice match between the PMA_2PbCl_4 2D MHP surface and the (020) β-CL-20 crystallographic plane, relative to the other bilayer pairs, which would suggest heterogeneous nucleation at the solution/ PMA_2PbCl_4 interface that is stabilizing these non-equilibrium orientations.

Recent work in the field of organic heteroepitaxial growth has suggested that the two requirements for organic–organic crystalline interfaces include similar lattice parameters and a preferred orientation of the lowest surface energy plane of the overlayer crystal.[27] However, our results suggest that more factors must be considered when investigating how organic crystalline surfaces influence nucleation and growth of bilayer organic crystalline structures.[27] Our findings indicate that, although the (002) and (020) preferential orientations are the lowest surface energy planes for the bulk β-CL-20 crystal, when organic molecules crystallize at an interface, we believe the primary consideration shifts from minimizing the bulk component surface energy to minimizing the interfacial energy.

To further elucidate the influence of the MGC technique and the 2D MHP template layer on the preferential

Table 1 Lattice fit parameter (m) between β-CL-20 crystallographic planes and 2D MHP unit cells

2D MHP Surface	$m_{(002)}$	$m_{(020)}$	$m_{(111)}$
PEA_2PbBr_4	0.2675	0.1703	**1.090**
PEA_2PbCl_4	0.2833	0.1779	**1.239**
PMA_2PbBr_4	0.9017	0.7033	**1.479**
PMA_2PbCl_4	1.081	**0.8637**	1.525

Experimentally observed results are indicated in **bold**. Lowest m value (closest lattice match) is indicated by green fill.

This journal is © The Royal Society of Chemistry 2024

React. Chem. Eng., 2024, **9**, 3248–3256 | **3253**

orientation, solvent vapor annealing (SVA) was utilized to remove effects of the MGC coating of the CL-20 crystal layer. SVA is commonly used to provide an energy input that allows for molecular mobility resulting in a relaxation of the crystalline material in a more thermodynamically stable configuration.[41,42] Upon recrystallization, the CL-20 crystals accumulated in a small region of the film (ESI† Fig. S11). Optical microscopy (ESI† Fig. S12) and AFM (ESI† Fig. S5) images of the crystalline regions show a different morphology and a slight decrease in nanoparticle size after SVA relative to the initial MGC coated CL-20 films. The CL-20 thin film does not exhibit stick–slip morphology after recrystallization from SVA, but instead tends to exhibit a bimodal distribution of crystal sizes (ESI† Fig. S12). Multiple morphologies were observed, including spherulitic, rod-like, and nanocrystalline morphologies.

Raman (ESI† Fig. S13) and x-ray diffraction (Fig. 4) data were collected after SVA, and films again preferentially crystallize as β-CL-20, but diffraction data collected demonstrates films tend to show much more variation in preferred crystallographic orientation after SVA than the original MGC bilayer films. To characterize the preferential orientation of CL-20 on different 2D MHP surfaces, the extent of preferential orientation for the crystallographic plane (*hkl*) is defined as: $\xi_{(hkl)} = [(hkl)$ peak intensity]/[sum of all peak intensity] where the peaks included in this analysis for CL-20 include scattering from the crystallographic planes highlighted in Fig. 4a.[43,44]

For the original films (pre-SVA), all show a preferential orientation ($\xi_{(111)} > 0.5$) of the (111) crystallographic plane, except for the PMA$_2$PbCl$_4$/CL-20 bilayer films, which show preferential (020) orientation (Fig. 4, solid points). The control Si and PMA$_2$PbBr$_4$ 2D MHP based bilayer films show an exceptionally high degree of (111) CL-20 orientation ($\xi_{(111)}$ = 1), while the PEA-based films show a moderate degree of preferential (111) orientation. SVA causes recrystallization so that a smaller area where CL-20 interacts with the 2D MHP template, resulting in thicker crystalline deposits. With this, we observe a lower degree of preferential orientation for the (111) plane (Fig. 4, open points), and a higher degree of preferential orientation for the (020) and (002) planes for the silicon, PMA$_2$PbBr$_4$, and PEA$_2$PbCl$_4$ films. These results suggest that due to the smaller area of interaction between the CL-20 and 2D MHP surfaces, the interface does not influence the nucleation and growth of the CL-20 crystals to the same extent as when MGC is employed. In other words, the degree of preferential orientation of CL-20 changes as the 2D MHP/CL-20 interaction area decreases. It is possible that CL-20 homogeneously nucleates from the amorphous phase and expresses a higher degree of the bulk stable (020) and (002) orientations rather than the interfaced stabilized (111) orientation observed after MGC.

Summary and conclusions

In this work, MGC was employed to crystallize CL-20 thin films on 2D metal halide 2D MHP templates to elucidate the influence of interfacial interactions on the crystallization of CL-20. Four 2D MHP surfaces were selected and compared to a silicon control. Small, non-uniform crystalline morphologies of CL-20 films were observed in all cases. Raman spectroscopy confirmed the formation of β-CL-20 for all films. The silicon, PMA$_2$PbBr$_4$, PEA$_2$PbCl$_4$, and PEA$_2$PbBr$_4$ templates induced a strong (111) preferential orientation of the CL-20 crystals, while the PMA$_2$PbCl$_4$ template induced a strong (020) preferential orientation of the CL-20 crystals. Pure, lattice matching based heteroepitaxial growth cannot
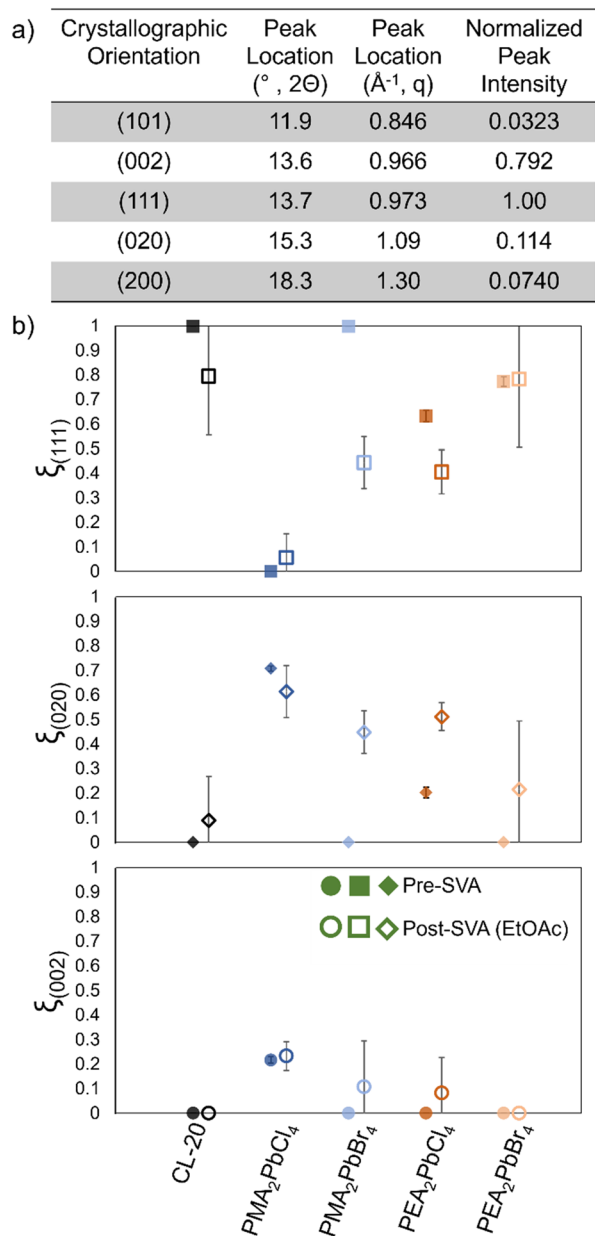

Fig. 4 a) Characteristic β-CL-20 diffraction peaks and normalized peak intensity calculated from .cif file.[1] b) extent of preferential orientation for (111), (020), and (002) planes of β-CL-20 prior to (filled in) and after (no fill) solvent vapor annealing with ethyl acetate for each perovskite/β-CL-20 bilayer film.

3254 | *React. Chem. Eng.*, 2024, **9**, 3248–3256

This journal is © The Royal Society of Chemistry 2024

explain the variable preferential orientation of the bilayer 2D MHP/β-CL-20 films; therefore, we hypothesize that minimization of interfacial energy is responsible for the observed various preferential orientations.

CL-20 thin films were recrystallized using solvent vapor annealing to probe interfacial interactions with 2D MHPs. After recrystallization, an accumulation of CL-20 particles on a small region of the film was observed, providing much lower area for interfacial interaction, accompanied by a higher degree of (020) orientation for the 2D MHP films and a lower degree of (111) orientation. This is consistent with an interfacial energy minimization between the template and overlayer crystalline planes that drives the formation of unique crystallographic orientations of the overlayer. This work suggests the importance of considering interfacial interactions when designing energetic material composites. Careful consideration and design of materials within EM composite formulations to account for possible changes in EM structure due to interfacial interactions will lead to enhanced design. Engineering composites to maintain predictable behaviour and stability in a variety of environments is crucial for effective and safe use.

Data availability

The data supporting this article have been included as part of the ESI.†

Author contributions

GG and NS initiated the work. NS made all samples and performed optical microscopy, Raman, and XRD characterizations. MP performed all profilometry measurements. All authors contributed to writing and revising manuscript.

Conflicts of interest

There are no conflicts to declare.

Acknowledgements

Notes and references

1 A. T. Nielsen, *et al.*, Synthesis of polyazapolycyclic caged polynitramines, *Tetrahedron*, 1998, **54**(39), 11793–11812.

2 A. Sider, *et al.*, Hexanitrohexaazaisowurtzitane or CL-20 in India: synthesis and characterisation, *Def. Sci. J.*, 2002, **52**(2), 135.

3 R. L. Simpson, *et al.*, CL-20 performance exceeds that of HMX and its sensitivity is moderate, *Propellants, Explos., Pyrotech.*, 1997, **22**(5), 249–255.

4 X. Sun, *et al.*, Phase Transition Routes for ε- and γ-CL-20 Crystals under High Pressures of up to 60 GPa, *J. Phys. Chem. C*, 2020, **124**(9), 5061–5068.

5 M. Ghosh, *et al.*, Understanding metastable phase transformation during crystallization of RDX, HMX and CL-20: experimental and DFT studies, *Phys. Chem. Chem. Phys.*, 2016, **18**(34), 23554–23571.

6 X. Zhou, *et al.*, Imparting high polymorph transition resistance to cyclotetramethylene-tetranitramine via spherulitic aggregation enabled crystal shape constraint, *Chem. Eng. J.*, 2023, **452**, 139602.

7 Z.-H. Xue, *et al.*, Layered assembling of energetic molecules with improved thermostability templated by in-situ generated 2D crosslinked macromolecules, *Chem. Eng. J.*, 2024, **489**, 151429.

8 N. Smith, *et al.*, Selective Morphological and Polymorphic Control of CL-20 Thin Films Using Meniscus-Guided Coating, *Cryst. Growth Des.*, 2021, **22**(2), 1164–1171.

9 S. M. Guthrie, *et al.*, Precipitation dominated thin films of acetaminophen fabricated by meniscus guided coating, *CrystEngComm*, 2022, **24**(2), 311–320.

10 S. Jung, *et al.*, Conductive, Large-Area, and Continuous 7,7,8,8-Tetracyanoquinodimethane@HKUST-1 Thin Films Fabricated Using Solution Shearing, *ACS Appl. Mater. Interfaces*, 2021, **13**(8), 10202–10209.

11 A. Ghorbanpour, *et al.*, Oriented UiO-66 thin films through solution shearing, *CrystEngComm*, 2018, **20**(3), 294–300.

12 D.-M. Smilgies, *et al.*, Look fast: Crystallization of conjugated molecules during solution shearing probed in-situ and in real time by X-ray scattering, *Phys. Status Solidi RRL*, 2013, **7**(3), 177–179.

13 G. Giri, *et al.*, Tuning charge transport in solution-sheared organic semiconductors using lattice strain, *Nature*, 2011, **480**, 504.

14 R. Hiremath, *et al.*, Controlling Molecular Crystal Polymorphism with Self-Assembled Monolayer Templates, *J. Am. Chem. Soc.*, 2005, **127**(51), 18321–18327.

15 J. F. Kang, *et al.*, Nucleation and growth of glycine crystals on self-assembled monolayers on gold, *Langmuir*, 2000, **16**(8), 3791–3796.

16 G. Toworfe, *et al.*, Nucleation and growth of calcium phosphate on amine-, carboxyl-and hydroxyl-silane self-assembled monolayers, *Biomaterials*, 2006, **27**(4), 631–642.

17 L. M. Frostman, M. M. Bader and M. D. Ward, Nucleation and growth of molecular crystals on self-assembled monolayers, *Langmuir*, 1994, **10**(2), 576–582.

18 E. Ruckenstein and Z. Li, Surface modification and functionalization through the self-assembled monolayer and graft polymerization, *Adv. Colloid Interface Sci.*, 2005, **113**(1), 43–63.

19 D. O. Hutchins, *et al.*, Effects of self-assembled monolayer structural order, surface homogeneity and surface energy on pentacene morphology and thin film transistor device performance, *J. Mater. Chem. C*, 2013, **1**(1), 101–113.

20 J. H. Urbelis and J. A. Swift, Solvent effects on the growth morphology and phase purity of CL-20, *Cryst. Growth Des.*, 2014, **14**(4), 1642–1649.

21 J. H. Urbelis, Altering physical properties of energertic materials and other small molecules through template-directed and co-crystallization methods, PhD, Georgetown University, 2014.

22 Y. Wang, *et al.*, Efficient α-CsPbI3 photovoltaics with surface terminated organic cations, *Joule*, 2018, **2**(10), 2065–2075.

23 C. C. Stoumpos, *et al.*, Ruddlesden–Popper hybrid lead iodide perovskite 2D homologous semiconductors, *Chem. Mater.*, 2016, **28**(8), 2852–2867.

24 X. Xiao, *et al.*, Unveiling Charge-Transfer Dynamics at Singlet Fission Layer/Hybrid Perovskite Interface, *ACS Appl. Mater. Interfaces*, 2023, **15**(31), 38049–38055.

25 A. M. Conley, *et al.*, Enhancing Organic Semiconductor Molecular Packing Using Perovskite Interfaces to Improve Singlet Fission, *Adv. Funct. Mater.*, 2023, **33**(47), 2303232.

26 M. Moret, *et al.*, Organic-organic heteroepitaxy: facts, concepts and perspectives, *Cryst. Res. Technol.*, 2011, **46**(8), 827–832.

27 J. T. Dull, *et al.*, Thin-Film Organic Heteroepitaxy, *Adv. Mater.*, 2023, **35**(35), 2302871.

28 M. Campione, *et al.*, Organic−Organic Epitaxy of Incommensurate Systems: Quaterthiophene on Potassium Hydrogen Phthalate Single Crystals, *J. Am. Chem. Soc.*, 2006, **128**(41), 13378–13387.

29 L. Raimondo, *et al.*, Epitaxial interfaces in rubrene thin film heterostructures, *J. Phys. Chem. C*, 2013, **117**(27), 13981–13988.

30 K. Momma and F. Izumi, VESTA 3 for three-dimensional visualization of crystal, volumetric and morphology data, *J. Appl. Crystallogr.*, 2011, **44**(6), 1272–1276.

31 W.-Q. Liao, *et al.*, A lead-halide perovskite molecular ferroelectric semiconductor, *Nat. Commun.*, 2015, **6**(1), 7338.

32 K.-Z. Du, *et al.*, Two-Dimensional Lead(II) Halide-Based Hybrid Perovskites Templated by Acene Alkylamines: Crystal Structures, Optical Properties, and Piezoelectricity, *Inorg. Chem.*, 2017, **56**(15), 9291–9302.

33 K. Thirumal, *et al.*, Morphology-independent stable white-light emission from self-assembled two-dimensional perovskites driven by strong exciton–phonon coupling to the organic framework, *Chem. Mater.*, 2017, **29**(9), 3947–3953.

34 K. Shibuya, *et al.*, Poly [bis (phenethylammonium) [dibromidoplumbate (II)]-di-μ-bromido], *Acta Crystallogr., Sect. E: Struct. Rep. Online*, 2009, **65**(11), m1323–m1324.

35 E. Von Holtz, *et al.*, The solubility of ε-CL-20 in selected materials, *Propellants, Explos., Pyrotech.*, 1994, **19**(4), 206–212.

36 S. M. Guthrie, D.-M. Smilgies and G. Giri, Controlling Polymorphism in Pharmaceutical Compounds Using Solution Shearing, *Cryst. Growth Des.*, 2018, **18**(2), 602–606.

37 I. Aranson, L. Tsimring and V. Vinokur, Stick-slip friction and nucleation dynamics of ultrathin liquid films, *Phys. Rev. B: Condens. Matter Mater. Phys.*, 2002, **65**(12), 125402.

38 P. A. Thompson and M. O. Robbins, Origin of stick-slip motion in boundary lubrication, *Science*, 1990, **250**(4982), 792–794.

39 M. Abo Jabal, *et al.*, Connecting monotonic and oscillatory motions of the meniscus of a volatile polymer solution to the transport of polymer coils and deposit morphology, *Langmuir*, 2018, **34**(39), 11784–11794.

40 P. Goede, N. V. Latypov and H. Östmark, Fourier Transform Raman Spectroscopy of the Four Crystallographic Phases of α, β, γ and ε 2, 4, 6, 8, 10, 12-Hexanitro-2, 4, 6, 8, 10, 12-hexaazatetracyclo [5.5. 0.05, 9.03, 11] dodecane (HNIW, CL-20), *Propellants, Explos., Pyrotech.*, 2004, **29**(4), 205–208.

41 G. Giri, *et al.*, One-dimensional self-confinement promotes polymorph selection in large-area organic semiconductor thin films, *Nat. Commun.*, 2014, **5**, 3573.

42 G. Giri, *et al.*, High-Mobility, Aligned Crystalline Domains of TIPS-pentacene with Metastable Polymorphs Through Lateral Confinement of Crystal Growth, *Adv. Mater.*, 2014, **26**(3), 487–493.

43 M. Kohga and H. Tsuzuki, Burning-Rate Characteristics of Composite Propellant Using Ammonium Perchlorate Modified by Ethylene Glycol, *J. Propul. Power*, 2011, **27**(3), 668–674.

44 M. Kohga and H. Tsuzuki, Crystal habit modification of ammonium perchlorate by ethylene glycol, *Adv. Powder Technol.*, 2010, **21**(4), 443–447.

3256 | *React. Chem. Eng.*, 2024, **9**, 3248–3256

This journal is © The Royal Society of Chemistry 2024